



A structural approach to 3D-printing arterial phantoms with physiologically comparable mechanical characteristics: Preliminary observations

Proc IMechE Part H:
J Engineering in Medicine
2022, Vol. 236(9) 1388–1402
© IMechE 2022

Article reuse guidelines:
sagepub.com/journals-permissions
DOI: 10.1177/09544119221114207
journals.sagepub.com/home/pih


Bruce Guest^{1,2} , Luis Arroyo³ and John Runciman¹

Abstract

Pulse wave behavior is important in cardiovascular pathophysiology and arterial phantoms are valuable for studying arterial function. The ability of phantoms to replicate complex arterial elasticity and anatomy is limited by available materials and techniques. The feasibility of improving phantom performance using functional structure designs producible with practical 3D printing technologies was investigated. A novel corrugated wall approach to separate phantom function from material properties was investigated with a series of designs printed from polyester-polyurethane using a low-cost open-source fused filament fabrication 3D printer. Nonpulsatile pressure-diameter data was collected, and a mock circulatory system was used to observe phantom pulse wave behavior and obtain pulse wave velocities. The measured range of nonpulsatile Peterson elastic strain modulus was 5.6–19 to 12.4–33.0 kPa over pressures of 5–35 mmHg for the most to least compliant designs respectively. Pulse wave velocities of 1.5–5 m s⁻¹ over mean pressures of 7–55 mmHg were observed, comparing favorably to reported in vivo pulmonary artery measurements of 1–4 m s⁻¹ across mammals. Phantoms stiffened with increasing pressure in a manner consistent with arteries, and phantom wall elasticity appeared to vary between designs. Using a functional structure approach, practical low-cost 3D-printed production of simple arterial phantoms with mechanical properties that closely match the pulmonary artery is possible. Further functional structure design development to expand the pressure range and physiologic utility of directly 3D-printed phantoms appears warranted.

Keywords

Arterial phantom, cardiovascular system mechanics, waveforms: hemodynamics, pulse wave, functional structure, physiologic elasticity, pulse wave velocity, 3D-printed phantom, additive manufacturing

Date received: 21 January 2022; accepted: 30 June 2022

Introduction

Waves drive blood through the arteries and there is a continuous energy exchange between pressure, flow, and arterial wall strain.^{1–3} Hemodynamics,^{4,5} particularly wave mechanics,^{6,7} are important in cardiovascular pathophysiology,⁸ however the basis of the arterial pulse wave has not been elucidated.¹ While arterial phantoms have value in pulse wave mechanics research,^{9–11} arterial architectural and nonlinear behavior complexities limit the utility of phantoms made from commercially available tubular elastomers.^{11–14} Although complex phantom architectures are producible with 3D printed mold techniques,¹⁵ practical direct 3D-printing of robust, distensible phantoms with

physiologically comparable properties suitable for studying wave mechanics is not reported.^{16–18} A major limitation is the cost and adaptability of the commercial 3D-printing elastomer technologies capable of printing complex geometries. Also, arteries stiffen with

¹School of Engineering, University of Guelph, Guelph, ON, Canada

²Ontario Veterinary College Health Sciences Centre, University of Guelph, Guelph, ON, Canada

³Department of Clinical Studies, Ontario Veterinary College, University of Guelph, Guelph, ON, Canada

Corresponding author:

Bruce Guest, School of Engineering, University of Guelph, 50 Stone Road East Guelph, Guelph, ON N1G 2W1, Canada.

Email: guestb@uoguelph.ca

increased distension^{19,20} in contrast to the generally linear elastic response of elastomers.

In simplistic terms, the most important aspects of a phantom used to study wave mechanics are wall mechanical properties, which determine speed of the pulse through strain energy storage and luminal morphology which determines wave reflection. The interaction of these two characteristics along with the amplitude and frequency of the inlet (driving) fluid pulse determine the behavior of the pulse wave.¹ Pulse wave velocity is generally conserved across mammals, with aortic values ranging from 4 to 13 m s⁻¹^{8,21–27} while pulmonary arterial velocities are reported in the range of 1–4 m s⁻¹.^{28–35} To have relevance in terms of pulse wave mechanics, an ideal phantom would exhibit physiologic wave speeds and forms at physiologic pressures. Systemic mammalian mean arterial pressures (mean/peak) are 100–120/120–140 mmHg and 160–180/180–220 mmHg at rest and exercise respectively,^{36–40} while pulmonary arterial pressures (mean/peak) ~double from 15 to 20 mmHg at rest to 25–40 mmHg during exercise in most species.^{41–45}

To ultimately obtain physiologic wave speeds and reflective behavior, our phantom development philosophy is to first develop simple 3D printable tubular phantoms with wall properties that replicate arterial mechanical behavior and then develop techniques to produce phantoms with the more complex shapes associated with physiologic wave reflection phenomena. As a first step, we sought to separate phantom function from the generally linear elastic inherent properties of 3D printing polymers by developing structural wall designs intended to produce mechanical properties similar to those of arteries.

In prior work, tubes with circumferential wall spring elements that reduced stiffness and imparted nonlinear elasticity were designed and then produced with a low-cost fused filament fabrication 3D-printing technique.⁴⁶ The objective of the current study was to determine if these tubes had properties suitable for the study of arterial wave mechanics. Pressure-diameter relationships were obtained, pulse wave velocity was measured over a range of pressures, and wave behavior was observed.

Methods

Phantom designs

Phantom circumferential elastic behavior was decoupled from the base material properties by using a spline function to generate the phantom circumference resulting in wall corrugations (Figure 1). Corrugation groove alignment with flow direction coupled with corrugation size to tube diameter ratios of < 0.05 suggests that corrugations would have little effect on fluid dynamic events associated with wave propagation.^{47,48} Previously, corrugated wall uniaxial behavior was found to be determined by corrugation size and pitch

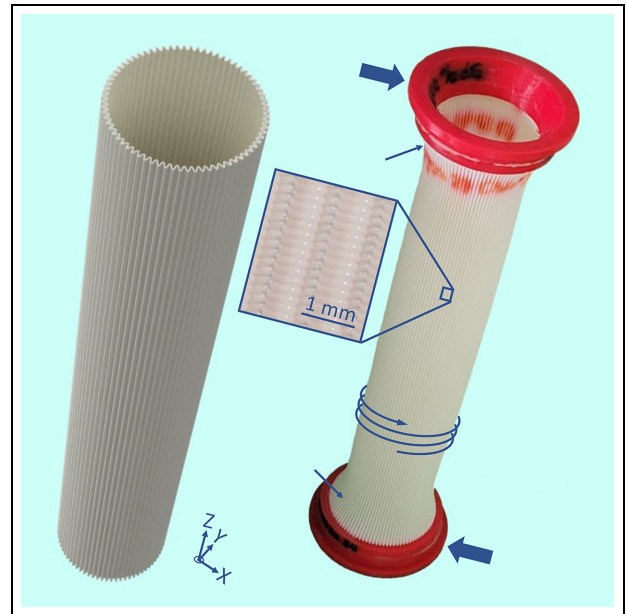


Figure 1. Rendered image of a corrugated phantom design (left) and an assembled 3D-printed phantom (right). Phantoms were printed progressively along their long (z) axis from a single thermally fused bead of polyurethane continuously extruded in a uniform corrugated pattern (inset) along a helical path (coiled arrow). 35 mm inner diameter polyurethane fittings (large arrows) were bonded to the phantom, expanding the ends (small arrows) and reducing phantom free length to 150 mm.

as well as wall thickness.⁴⁶ To estimate the potential performance range of the structural-function approach, five corrugated designs differing by one or more of corrugation size, pitch or wall thickness were evaluated along with a smooth wall design for comparison to typical phantom constructs. One phantom of each design was produced from polyester-polyurethane (Elastollan[®] BASF, Germany) based filament (TPU-60A Spool3D, Canada) using previously described techniques.⁴⁶ Phantoms were printed to a height of 160 and 35 mm ID polyurethane end fittings were bonded, via polyurethane contact cement, reducing long axis free length to 150 mm (Figure 1). Due to thermal contraction inherent in fused filament printing and wall flexion during the printing process, printed corrugation size was smaller and wall thickness greater than the design parameters. As-printed phantom parameters are detailed in Table 1 and phantom cross-sectional scans of the corrugated phantoms are shown in Figure 2.

Pressure-diameter

Phantoms were horizontally mounted between the inlet and central bulkheads of a rail mount system. The central bulkhead was mobile, allowing adjustment of the phantom installed length. To avoid buckling⁴⁹ during luminal pressurization, the free phantom length between end fitting inner faces was fixed at 160 mm resulting in ~ 10 mm pretension ($\lambda_{zz} \sim 1.07$) for all

Table 1. As-printed phantom parameters.

Design type	Nominal diameter (mm)	Circumferential corrugation count	Corrugation pitch (mm)	Corrugation size (mm)		Wall thickness (mm)	
				Mean	SD	Mean	SD
A	35	None	-	-	-	0.240	0.009
D	35	48	2.291	1.523	0.021	0.276	0.014
E	27	60	1.412	0.915	0.010	0.239	0.006
F	27	72	1.178	0.935	0.015	0.248	0.009
G	27	96	0.884	0.892	0.014	0.213	0.011
H	27	96	0.884	1.103	0.020	0.227	0.008

Morphometric analysis of scanned images used to estimate corrugation size (10 measures) and wall thickness (20 measures). Corrugation pitch determined from nominal diameter and size is distance between inner and outer corrugation apices (see Figure 2). As designs E–H were anticipated to be more distensible, a smaller diameter was used to better match phantom lumen diameter at lower pressures to that of the pulsatile test system piping.

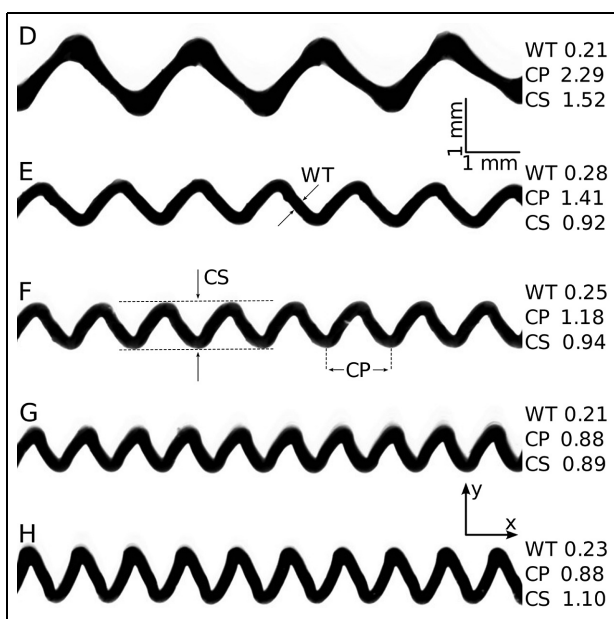


Figure 2. As printed corrugated wall designs. Images obtained by flatbed optical scanning of straightened unstrained phantom sections (~10 mm in length) cut in x-y plane at 30 mm build height, irregularities on and along section edges are associated with cutting artifacts. Letters denote design type, note variations in pitch between D through G and amplitude between D and H, complete metrics in Table 1. Scale bar applies to all sections. WT: wall thickness (mm); CP: corrugation pitch (mm); CS: corrugation size (mm).

designs. To avoid sagging when filled, phantoms were immersed in an open water filled trough attached to the inlet and outlet bulkheads (Figure 3(a)). A large-bore water manometer in conjunction with sequential manual operation of ball valves located in tubing connected to the inlet and outlet bulkheads was used to pressurize the phantoms (Figure 3(b)–(d)) over a 40–60 s period to near steady state followed by a 10–20 s period of depressurization. During each pressure/depressurization cycle diameter was measured with a laser micrometer (LS9120 Keyence, Canada) positioned at the mid axial length (80 mm from the inner face of the inlet end fitting) for all phantoms. Additionally, to

objectively demonstrate axial anisotropy and end constraint effects, design G was surveyed along its entire length in 5 mm increments. Pressure was measured via an electronic pressure catheter (FTS-5011B-0048D, Transonic-Scisense Inc. Canada) positioned at the phantom long axis and radial midlines. Signals were recorded at 100 sps with a data acquisition system (DT9826, Measurement Computing Corporation, USA).

Data were collected from five pressure/depressurize cycles over a single pressure range for the essentially linear response smooth walled design and over two pressure ranges for the corrugated designs. Corrugated phantoms were first pressurized to a diametrical strain beyond the uniaxial nonlinear elastic response previously established,⁴⁶ then to optimize resolution of Peterson elastic strain modulus determination within the physiologic response envelope, a lower charging pressure just exceeding the linear range of the calculated elastance response was used. Phantoms were preconditioned with four to six pressure/depressurize cycles until the end pressurization manometer height varied < 2 mm between successive cycles. Strain/destrain rates were an uncontrolled consequence of the manometer charge start height, inlet and outlet tubing diameters and lengths, manual valve operation rates and phantom compliance.

Raw pressure and diameter data were filtered with a Savitzky-Golay⁵⁰ filter and independently differentiated (after Parker³) with respect to time by convoluting each signal with its first order Savitzky-Golay derived differentiation filter.⁵¹ Elastance ($dP \cdot dD^{-1}$) and compliance ($dD \cdot dP^{-1}$) differentials were obtained by both Savitzky-Golay convolution and direct sample-to-sample difference methods. An additional Savitzky-Golay filter was applied post differentiation to the Savitzky-Golay convolution method but not to the direct method differentials. Savitzky-Golay method differentiation and post differentiation filter parameters were recursively adjusted to minimize distortion of the smoothed Savitzky-Golay method results relative to the direct method (Supplemental Figure 1). Optimized results from the Savitzky-Golay method were used for

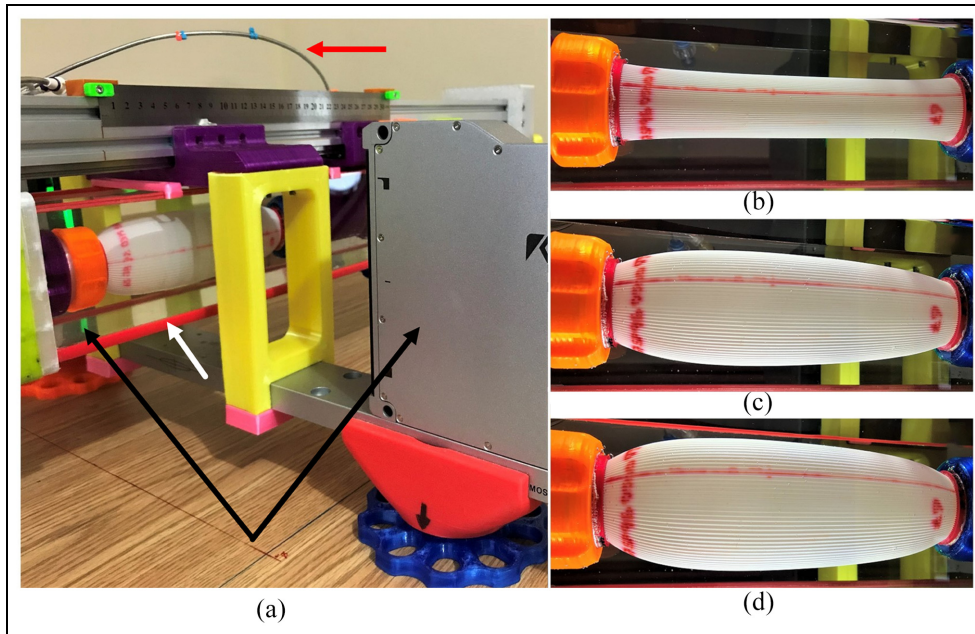


Figure 3. Pressure-diameter test setup. Laser micrometer attached to phantom rail mount system (a), laser transmitter and receiver (black arrows), support medium open trough (white arrow), pressure catheter introducer sheath (red arrow). Phantom pressurization images captured during at 3, 30, and 45 mmHg ((b–d) respectively).

Table 2. Diametrical strain parameters at phantom axial midpoint.

Design type	Pressure range (mmHg)		Strain Maximum		Strain rate ($s^{-1} \times 10^{-2}$)	
	Start	End	Mean	SD	Mean	SD
A	5	90	0.21	0.015	5.57	0.137
D	7	75	0.37	0.002	4.53	0.302
D	10	50	0.24	0.011	5.77	0.148
E	3	70	0.65	0.001	6.12	0.005
E	5	45	0.45	0.001	7.68	0.197
F	3	70	0.88	0.002	5.30	0.008
F	5	45	0.61	0.002	6.53	0.020
G	3	65	1.00	0.007	5.00	0.018
G	5	45	0.66	0.005	5.55	0.008
H	3	63	1.16	0.012	4.27	0.025
H	5	45	0.91	0.004	4.47	0.001

Strain rate mean and standard deviation across analytical groups at 80 mm axial distance is $5.53 \pm 1.01 s^{-1} \times 10^{-2}$ respectively. Data recorded 80 mm from phantom inlet.

analysis. Analyzed pressure ranges and strain parameters are presented in Table 2.

Pulsatile behavior

A water-based ex-vivo equine lung perfusion mock circulatory system,⁵² modified to house the rail mount system and improve pulse wave generation capability, was used to observe pulsatile behavior and determine pulse wave velocity (Figure 4). Briefly, a microcontroller-based pulse engine operated a pulse generation ball valve via a stepper motor (STM24QF-3AE Applied Motion Products Inc., USA) using closed loop servo positioning. A centrifugal pump drawing from a main

reservoir generated system pressure. Pulse valve feed pressure was regulated by upstream bypass and inlet valves, which remained in fixed positions. Fluid and mechanical impulses were damped with a 360° flexible hose loop attached to a rubber and metal element between the bypass valve and inlet valves. Downstream of the pulse valve there was a magnetic flow meter (SM6000 ifm efector, Canada), a temperature indicator and a pressure transmitter for an over pressure protection system. The rail mount inlet bulkhead contained a check valve and there was a flat faced flow restriction element at the phantom outlet. A resistance valve, under open loop pulse engine control, was connected to the outlet bulkhead by flexible tubing. An anti-surge

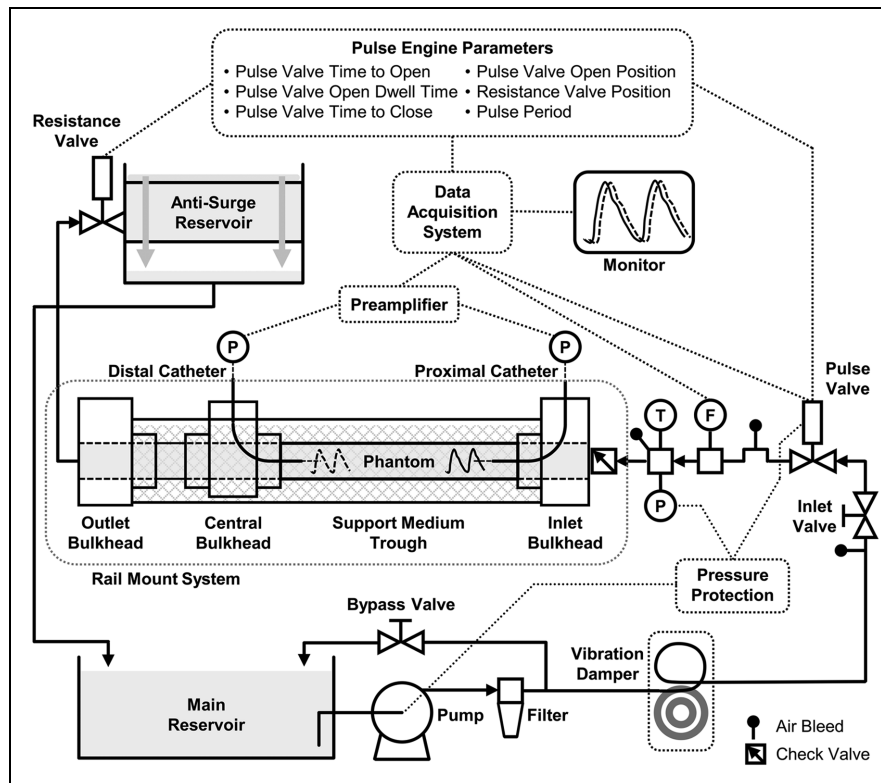


Figure 4. Schematic representation of mock circulatory system. A microcontroller-based pulse engine generates repeatable fluid pulses by controlling pulse valve open position, open and close rates and open dwell time as well as pulse period and resistance valve position. Anti-surge reservoir spill over height determines terminal runoff pressure. Phantom is horizontally mounted via rail mounted bulkheads and supported in water trough. Data acquisition system records proximal and distal intraluminal pressures, inlet flow rate and pulse valve position. Pump vibrations and water hammer impulses are damped by a looped hose fixed to a rubber and metal element. Protection system prevents phantom over-pressurization. P: pressure; T: temperature; F: flow.

reservoir with its spillover height set 50 mm above the phantom long axis midline was directly connected to the resistance valve.

Five Fr electronic pressure catheters (FTS-5011B-0048D, Transonic-Scisense Inc. Canada) were passed through 9 Fr introducer sheaths (CL-07900 Arrow International Inc, USA) contained within low clearance guide tubes built into the rail mount system inlet and central bulkheads. Relative motion between the catheters and introducer sheaths was eliminated by a locking plug inserted between them with catheter protrusion fixed at 30 mm to minimize motion and introducer sheath flow disturbance. The central bulkhead was positioned to create a 160 mm inter flange phantom length, generating ~ 10 mm prestretch. The catheter sensing elements were positioned before phantom installation with a gage block mounted, mm graduated, rule after which the introducer sheaths were fixed in place via gland fittings at the bulkhead guide tube entrances. This arrangement precisely located the sensing elements relative to the phantom ends and each other and allowed accurate repositioning by advancing or retracting the introducer sheaths within the bulkhead guide tubes. During pulse wave velocity data collection, the proximal and distal pressure sensors were placed

30 mm from the inlet and outlet ends of the phantom respectively, resulting in 100 mm sensor separation. At this spacing the introducer sheath ends were flush with the rigid guide tube outlets minimizing catheter motion induced signal noise.

Pulse valve open position, time to reach open position, dwell time at open position, time to close, pulse frequency and static resistance valve position were controlled by the pulse engine. These parameters formed a pulse profile which, along with the bypass and inlet valve positions, anti-surge reservoir height and phantom mechanical properties determined pulse wave characteristics. Nine pulse profiles were developed (Table 3) to produce a range of five mean wave pressures (example Figure 5(a)) in each design and optimize wave foot transition clarity. Pulse wave velocity was calculated from wave foot minimum fiduciary points⁵³ and by statistical phase offset⁵⁴ applied to an analysis window selected to encompass a region of proximal and distal wave shape similarity in the runoff phase. Design G pulse profile 2 wave behavior was characterized with sequential data obtained by positioning the pressure sensors at the phantom long axis midpoint then retracting by 5 mm increments until sensors were 5 mm from each phantom end.

Table 3. Pulse engine pulse profiles.

Pulse profile number	Pulse valve open time (ms)	Pulse valve dwell time (ms)	Pulse valve close time (ms)	Pulse period (ms)	Maximum pulse valve position (%)	Resistance valve position (%)
1 ^a	150	20	150	1000	50	30
2 ^b	126	25	200	2000	60	14
3 ^b	250	50	200	2000	60	14
4 ^b	255	63	255	2000	85	12
5 ^b	255	63	255	2000	90	10
6 ^c	200	50	225	1008	40	9
7 ^c	200	50	225	1008	60	9
8 ^c	200	50	225	1008	80	9
9 ^c	200	50	225	1008	100	9

^aAll designs.

^bDesigns D through H.

^cDesign A.

Electrical, fluid dynamic and mechanical noise were reduced by collecting data in 50 wave sets and analyzing the time synchronous ensemble average⁵⁵ of the individual pressure waves (Supplemental Figure 4), inlet flows and pulse valve positions. All signals were sampled at 10ksps and the data acquisition system (DT9826, Measurement Computing Corporation, USA) received a synchronizing signal from the pulse engine. Savitzky-Golay filtration was applied to individual and ensemble data. Pressure signals were preamplified (FP895B Transonic-Scisense Inc, Canada) and temperature drift was compensated by matching no flow pressures to anti-surge reservoir height. After initiating pulsatile flow, data collection commenced once the pulse wave form stabilized. Water temperature was recorded manually for each wave set. Design G relationships between pulse profiles and resultant pressure waves are shown in Figure 5(b) to (f).

Results

Pressure-diameter

Compliance on 5 mmHg pressure isobars along the long axis of design G demonstrate longitudinal anisotropy, circumferential nonlinearity and end constraint effects (Figure 6). Design A (smooth wall) was considerably stiffer than the corrugated designs and its elastance response was near linear at lower pressures but declined at pressures $> \sim 50$ mmHg versus corrugated designs which stiffened with increasing pressure up to ~ 30 – 50 mmHg (Figure 7(a)). Over pressures of ~ 5 – 35 mmHg, the non-pulsatile Peterson elastic strain modulus of the corrugated designs increased with increased pressure, ranging from ~ 5.6 – 19.0 to ~ 12.4 – 35.1 kPa for the most to least compliant designs respectively and differences in Peterson elastic strain moduli between designs were consistent with respective differences in elastance response (Figure 7).

Pulsatile behavior

Minimum wave pressure (pressure at end of runoff phase), pulse pressure (difference between minimum and maximum wave pressures), pulse volume, maximum inlet flow rate and water temperature data over five pulse profiles for all designs are shown in Table 4.

Pulse pressure and volume relationships relative to minimum wave pressure appeared to vary between design types (Figure 8). Design A had smaller pulse pressures and pulse volumes relative to minimum pressures compared to corrugated designs and pulse pressure declined slightly with increasing minimum pressure versus the corrugated designs which demonstrated increased pulse pressure with increased minimum pressure. Corrugated design pulse volume response to increased pressure was blunted at the highest-pressure pulse profile. Pulse pressure normalized pulse volume response when normalized to corrugation number ($R^2 = 0.79$, $p < 0.01$) and when normalized to corrugation number, likely proportional to corrugation size (Figure 8(b)).

Pulse wave velocity, as determined by foot-of-wave fiduciary point (Figure 9(a)), in the corrugated designs increased with mean wave pressure (~ 1.5 – 5 m s^{-1} / ~ 7 – 55 mmHg respectively) compared to the smooth wall design in which pulse wave velocity decreased with increasing mean wave pressure (~ 10 – 5.5 m s^{-1} / ~ 10 – 75 mmHg respectively). Foot-of-wave pulse wave velocity analysis did not clearly identify differences between corrugated designs, however pulse wave velocity of the secondary wave in the runoff phase did appear to differ with designs (Figure 9(b)). Over mean analysis window pressures of ~ 5 – 65 mmHg corrugated phantom pulse wave velocities determined by statistical phase offset varied from ~ 1.4 to 3.1 m s^{-1} respectively and there appeared to be a consistent inverse relationship between size and number of corrugations and pulse wave velocity across designs (Figure 9(b)).

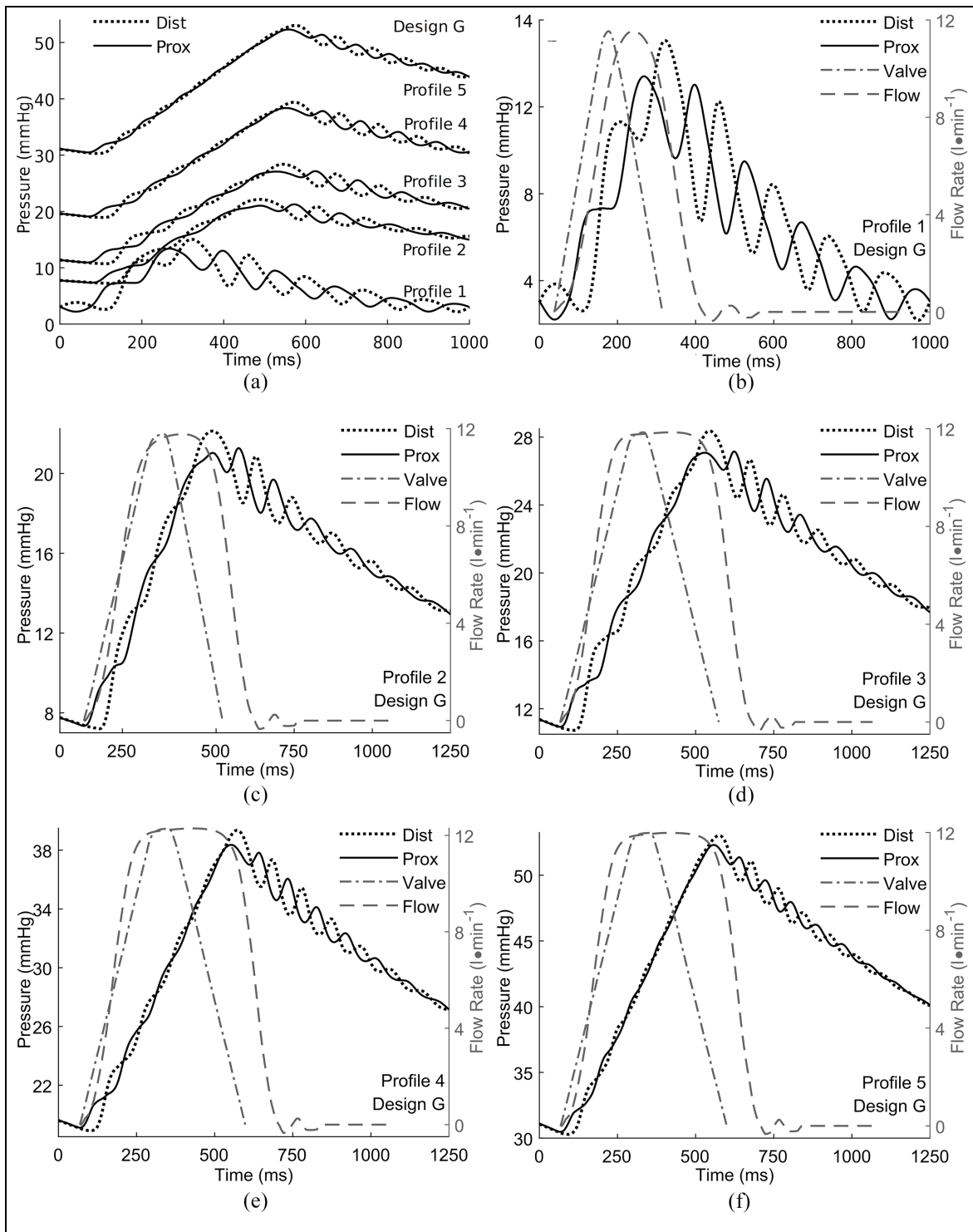


Figure 5. Design G pulse profile and wave relationships. Distal and proximal pressure waves (recorded 30 mm from the respective phantom ends) for five pulse profiles (a), first 1000 ms of profiles 2 through 5 shown. Individual pulse profiles (b–f) with inlet flow onset and pulse valve open transition synchronized to proximal pressure wave foot, first 1250 ms of profiles 2 through 5 shown. Pulse valve position normalized to flow rate. Two phases of the main pressure wave are defined; an inflow phase while the pulse valve (dash-dot line) is open and a runoff phase during the period of pulse valve closure (b–f). Note the secondary wave superimposed on the main pressure wave forms, please refer to Figure 10 for a temporal-spatial depiction and the discussion for a proposed explanation.

A combined temporal and spatial interpolation of design G, pulse profile 2 pressure wave demonstrates shape variation along the phantom long axis (Figure 10).

Discussion

Long axis compliance anisotropy (Figure 6) limits the functional length of fused filament fabrication

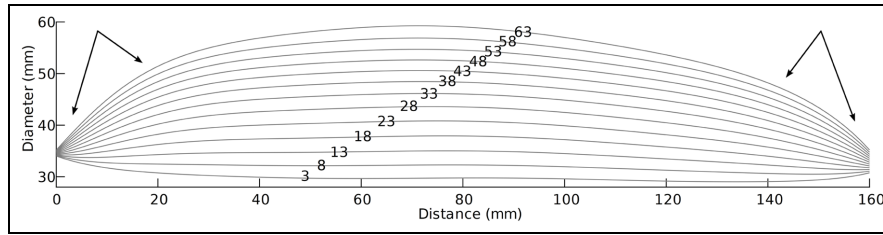


Figure 6. Nonpulsatile compliance on pressure isobars along design G long axis. Isobar values indicated (mmHg); diameter and distance scales are equivalent. Upper build height end of phantom (oriented at 0 mm distance) appears more compliant than build surface end. Compliance becomes non-physiological (increasing with increasing pressure) at luminal pressures above ~50 mmHg. Phantom effective reflective distance decreases and end reflective site abruptness increases with increasing pressure (arrows). Nominal end diameters constrained to 35 mm by fittings. Data generated from polynomial fit of pressure and diameter measurements obtained at 5 cm intervals along long axis.

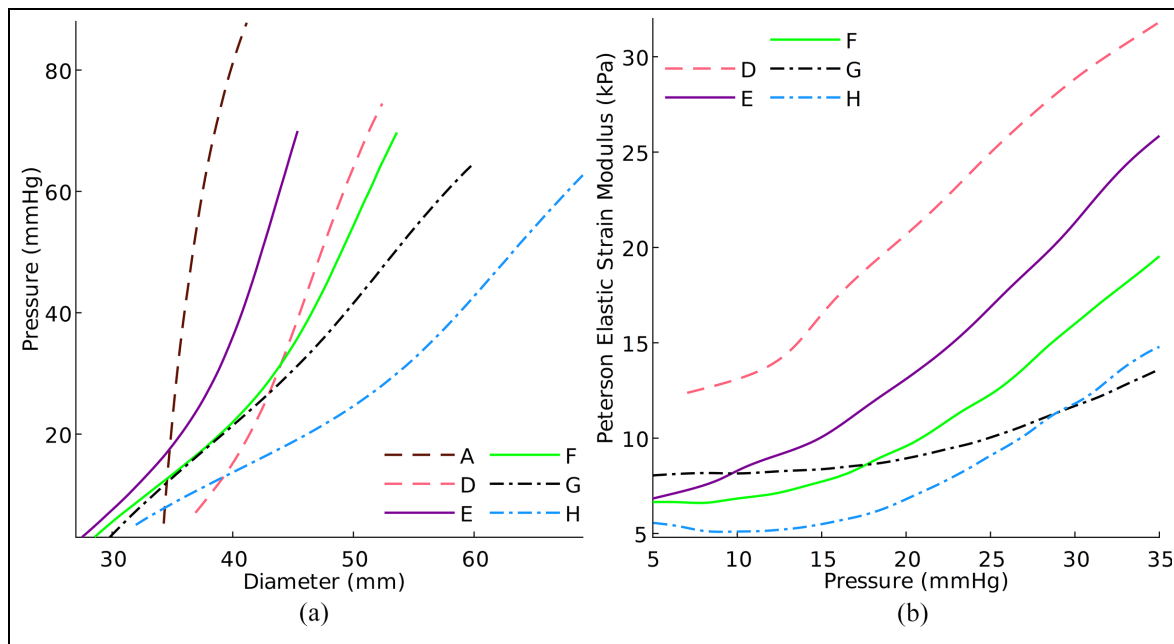


Figure 7. Analysis of five repeated pressure-diameter measures at mid phantom long axis distance (80 mm from inlet); (a) elastance (all designs) and (b) non-pulsatile Peterson elastic strain modulus (corrugated designs). Cursory analysis of standard deviation (see Supplemental Figures 2 and 3) indicates nonlinearity and significant difference between phantoms. Note difference in design A (smooth wall) elastance magnitude and slope compared to corrugated designs (D–H). Letters denote design types.

phantoms and occurs due to wall instability, which increases with build height, causing corrugation shape alteration during the printing process.⁴⁶ The zone of diametrical reduction associated with the end fittings approaches 20% of phantom length at higher pressures (Figure 6). While the inlet transition zone is analogous to aortic and pulmonary artery–heart base junctures, the outlet zone is not representative of distal arterial branching and transitional compliance. Increasing functional length and developing a more physiologic outlet termination will potentially improve phantom utility, particularly regarding wave behavior.

Corrugated phantom Peterson elastic strain moduli (Figure 7(b)) ranged from 5.6 to 19 kPa to 12.4 to 33.0 kPa over pressures of 5–35 mmHg for the most to least compliant design types respectively. In vivo

Peterson elastic strain modulus in calves was found to be ~41 kPa at a mean pressure of ~64 kPa,⁵⁶ while inflation testing of mouse pulmonary artery over 5–40 mmHg found a Hudetz’s modulus of ~27 kPa.⁵⁷ As pressure-diameter testing strain rates (Table 2) were considerably lower (mean $\sim 5.5 \text{ s}^{-1} \times 10^{-2}$) than estimated pulsatile strain rates ($1\text{--}2 \text{ s}^{-1}$), reported pressure-diameter data should be considered non-pulsatile and more comparable to inflation testing, versus typical in vivo Peterson elastic strain modulus data. The effectively concurrent distension along the phantom long axis during pressure-diameter testing would be expected to yield a lower elastic modulus compared to a traveling pulse wave, as constraint imposed by the downstream, and to a lesser extent upstream, undilated adjacent wall would be absent during nonpulsatile conditions. Also,

Table 4. Pressure and flow response of phantoms to a range of pulsatile flow inputs.

Design A											
Design D											
Pulse profile	P _{Min} (mmHg)	P _{Pulse} (mmHg)	V (ml)	Q _{Max} (l·min ⁻¹)	T (°C)	Pulse profile	P _{Min} (mmHg)	P _{Pulse} (mmHg)	V (ml)	Q _{Max} (l·min ⁻¹)	T (°C)
1	1.1	9.90	39	11.4	30.9	1	3.0	11.1	40.2	11.7	28.9
6	20.2	7.46	52.6	10.5	31.5	2	9.7	23.3	69.9	12.1	29.1
7	38.4	6.90	64.7	10.8	31.5	3	13.3	30.8	85.8	12.1	29.3
8	52.1	5.68	69.9	10.7	31.5	4	22.6	35.1	87.9	11.8	29.3
9	61.4	5.24	74.0	10.7	31.6	5	41.3	31.8	85.8	11.4	29.4
Design E											
Design F											
Pulse profile	P _{Min} (mmHg)	P _{Pulse} (mmHg)	V (ml)	Q _{Max} (l·min ⁻¹)	T (°C)	Pulse profile	P _{Min} (mmHg)	P _{Pulse} (mmHg)	V (ml)	Q _{Max} (l·min ⁻¹)	T (°C)
1	2.6	12.6	41.5	12.4	25.8	1	3.1	11.3	46.9	14.3	32.2
2	10.2	22.9	69.5	12.1	26.3	2	14.4	19.3	82.8	14.9	32.1
3	14.1	32.3	86.1	12.1	26.7	3	20.0	28.2	103.3	15.0	32.0
4	22.9	40.8	88.0	11.9	27.7	4	23.6	31.1	107.3	14.9	32.0
5	41.5	41.6	85.6	11.4	27.3	5	31.0	32.1	107.3	14.6	31.9
Design G											
Design H											
Pulse Profile	P _{Min} (mmHg)	P _{Pulse} (mmHg)	V (ml)	Q _{Max} (l·min ⁻¹)	T (°C)	Pulse Profile	P _{Min} (mmHg)	P _{Pulse} (mmHg)	V (ml)	Q _{Max} (l·min ⁻¹)	T (°C)
1	2.2	12.0	39.1	11.5	35.9	1	3.4	9.2	45.1	13.8	27.8
2	7.3	14.4	68.3	11.8	35.3	2	15.0	10.5	80.0	14.3	27.9
3	10.8	16.9	84.5	11.9	35.0	3	21.7	14.5	100.0	14.5	28.2
4	19.0	19.8	91.1	12.3	34.5	4	36.3	17.9	105.9	14.7	28.5
5	30.4	22.3	90.1	12.0	34.2	5	49.8	14.9	105.5	14.4	28.8

P_{Min}: minimum pressure; P_{Pulse}: pulse pressure; V: pulse volume; Q_{Max}: maximum pulse flow rate; T: fluid inlet temperature during data collection.

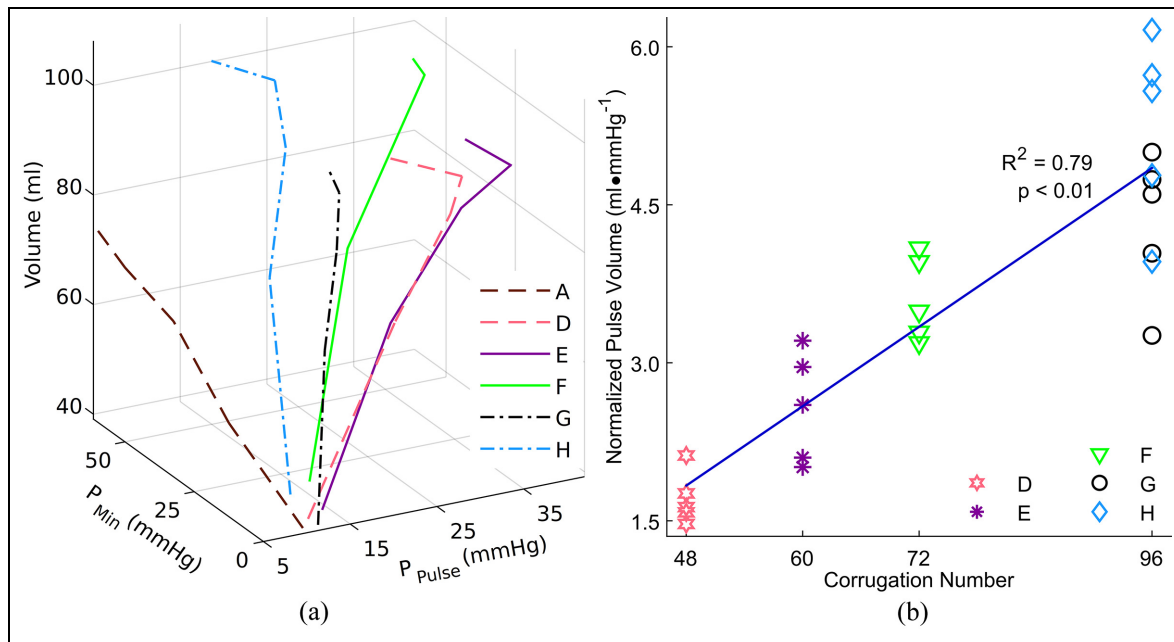


Figure 8. Phantom pulse volumes relative to pulse pressure and minimum wave pressure (a). Data obtained from five pulse profiles for each design (Table 4), letters denote design types. Pulse pressure of design A (smooth wall) phantom is small compared to corrugated designs and declines with increasing minimum pressure in contrast to corrugated designs where pulse pressure tends to increase with increasing minimum pressure except for the highest-pressure pulse profile where pulse pressures are essentially unchanged. Pulse volume response, normalized to pulse pressure and corrugation magnitude, relative to corrugation number of corrugated phantoms (b) over five different pulse profiles. For corrugated designs, normalized pulse volume appears to vary by design type with normalized pulse volume correlated to corrugation number and, comparing designs G and H, is also likely proportional to corrugation size.

the markedly lower strain rates compared to pulsatile conditions would be expected to result in decreased slope of the elastic response due to reduced viscoelastic effects. Consequently, the pressure-diameter method used should overestimate phantom compliance.

Elastance of the corrugated phantoms was nonlinear and markedly lower than the smooth walled design (Figure 7(a)). However, at higher pressures, likely due to a purely elastomeric material response as the corrugated spring elements become fully extended, corrugated design elastance becomes linear. This transition identifies the upper pressure limit of the physiologic response range for each design. The compromise between higher compliance and physiologic response range is evident from the corrugated phantom Peterson elastic strain moduli (Figure 7(b)); the modulus of design H is half that of design E but the slope declines at ~23 mmHg pressure versus design E which maintains a physiologic profile to 35 mmHg. Both elastance and Peterson elastic strain modulus of the corrugated designs appear to have an inverse relationship to corrugation number or corrugation size.

Maximum inlet convective velocities (derived from volumetric flow rate, Table 4) ranged from ~0.17–0.23 m s⁻¹ across all designs and pulse profiles, suggesting that convective flow was not a significant contributor to pulse wave velocity. Variations in maximum flow rates were consistent with volume differences between pulse

profiles within design types (Table 4) but lack of concurrent diameter data precludes analysis of reservoir function within and between designs. Corrugated phantom pulse volumes and pulse pressures appeared to vary between designs and were larger than the smooth wall design (Table 4, Figure 8(a)). Pulse volumes were largest in designs F and H and were similar across pulse profiles, but the less compliant design F generated nearly twice the pulse pressures as design H while pulse pressures in designs D and E were highest, pulse volumes were similar between them (Table 4, Figure 8(a)). The pulse volume was unchanged in design F and decreased in all other corrugated designs for pulse profile 5 versus 4 despite increased maximum pressure (Table 4). Increased outlet resistance via the resistance valve or increased elastance associated with higher pressure (Figure 7(a)) or both may have caused this effect. The inter phantom volume and pressure variations observed suggest design-based differences in reservoir behavior and pulse volume normalized to pulse pressure and corrugation size was found to be correlated to number of corrugations (Figure 8(b)).

Design A pulse wave velocity was fastest (~10 m s⁻¹ at a mean wave pressure of ~10 mmHg), as predicted by its elastance (Figure 7(a)) and declined to ~5 m s⁻¹ when the mean wave pressure was ~77 mmHg (Figure 9). This non-physiologic response⁵⁸ is expected for a smooth wall phantom as the base material elasticity decreases with stretch (Figure 7(a)) while the wall

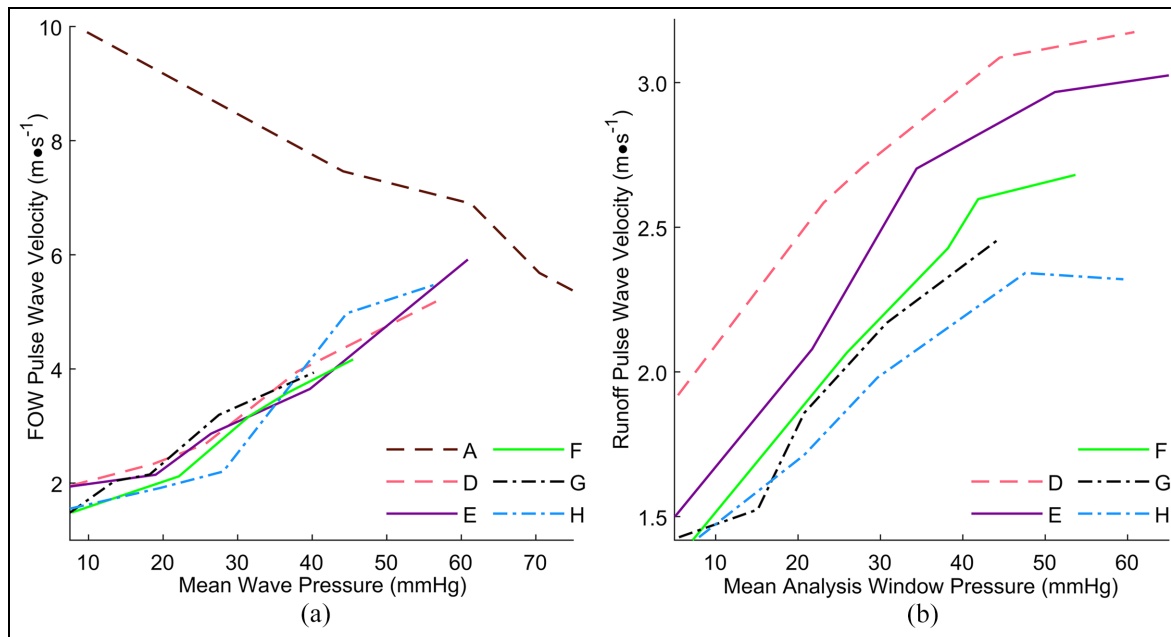


Figure 9. Relationship between phantom pulse wave velocity and mean wave pressure for pulse wave velocities obtained from foot-of-wave (FOW) fiduciary point analysis (a) and from statistical phase offset analysis of waves present in the runoff phase (b). Letters denote design types. In contrast to the smooth wall phantom (A), pulse wave velocity determined by foot-of-wave analysis for the corrugated phantoms (D–H) increases with increasing pressure. Corrugated phantom pulse wave velocities determined by foot-of-wave analysis are similar for all designs whereas wave velocities during runoff appear to have an inverse relationship to corrugation number or size.

(hoop) stress increases directly with diameter and inversely with thickness.⁵⁹ The non-physiological pulse wave response of smooth wall phantoms is also predicted by the Moens-Korteweg equation which defines a proportional relationship between pulse wave velocity and the square root resulting from the product of the incremental elastic modulus and wall thickness divided by the tube radius.^{19,26,60} Conversely, corrugated phantom pulse wave velocities increased with increasing pressure (Figure 9) in a physiologically consistent manner within their respective nonlinear response ranges (Figure 7). Pulse wave velocities obtained were $\sim 1.4\text{--}5\text{ m s}^{-1}$ over mean wave pressures ranging from 7 to 45 mmHg respectively for speed at the foot of the wave and of ~ 1.4 to $\sim 3.4\text{ m s}^{-1}$ over runoff analysis window mean pressures of $\sim 4\text{--}45$ mmHg respectively (Figure 9).

Interestingly, runoff wave velocity appeared to better differentiate corrugated design type versus foot-of-wave velocity (Figure 9), and the differentiation matches the relative speed differences anticipated from the design parameters (decreased stiffness with increased corrugation number and/or corrugation size) and predicted by the pressure-diameter testing (Figure 6). The differences in pulse wave velocity differentiation of design types between the analysis methods may be a consequence of reduced fluid dynamic environment complexity during runoff, where flow wave effects and rapid changes of wall stiffness are minimized. While regions of waveform similarity between distal and proximal waves in the runoff phase were found for most phantom and pulse

profile combinations, differences were observable which may have affected accuracy of the statistical phase offset technique.^{53,61} Pulse wave velocity variation throughout the evolution of the pulse wave in time and distance also needs to be considered.⁶²

Secondary wave (Figure 5) characteristics are illuminated by the temporal-spatial pressure wave representation (Figure 10). The near uniform periodicity and remarkable attenuation of the superimposed wave at phantom mid length suggests that it may be a trapped reflected wave. Wave trapping is expected given the relatively short phantom length and powerful reflective sites⁶³ arising from the abruptly reduced diameter and increased stiffness (Figure 6) associated with the phantom end fittings. Considering the temporal-spatial totality of the pressure wave (Figure 10) in conjunction with inlet fluid pulse timing (Figure 5) suggests a basis for the shape of the pressure wave. The main wave results from the pressure rise generated by inlet fluid pulse momentum working against the outflow resistance. The springs formed by the phantom wall corrugations are stretched by the pressure and moderate the pressure rise rate and magnitude by storing fluid volume and strain energy. As inlet flow ceases, spring strain energy is released, driving out the stored volume, resulting in gradual pressure attenuation. A second presumably persistent reflected wave appears early in the inflow phase and is superimposed on the main wave. Based on the observed pressure-flow behavior, it seems likely that exposing a series of phantoms with different

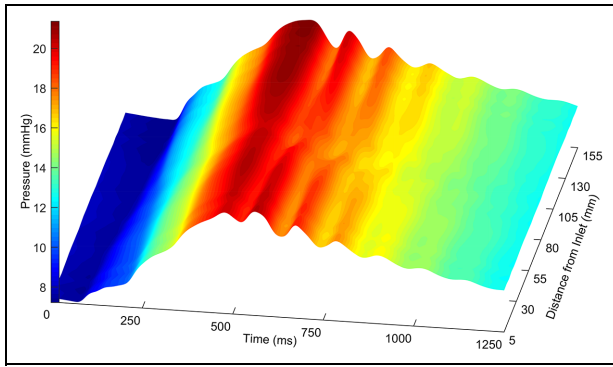


Figure 10. Interpolation of repeated pressure waves surveyed along phantom long axis in 5 mm increments from inlet. First 1250 of 2000 ms pulse duration shown. Note attenuation of secondary wave at phantom midpoint (80 mm distance). Design G, pulse profile 2.

mechanical and reflective properties to a range of precisely repeatable inlet fluid pulses while measuring pressure, flow, and diameter along the length of the phantoms would support further development of wave intensity³ and reservoir function³¹ analysis. This approach may provide new insights into the mechanistic basis of the pulse wave.

Multiple copies of each design type were not produced, and repeated measures were not obtained for pulsatile data, consequently results cannot be stated with statistical confidence. However, based on the relatively simple and automated nature of the 3D printing process and the reproducibility observed during the development process, it is reasonable to expect repeatability of corrugation form and function within design types in future trials. In this study, the corrugated designs were consistently differentiated by corrugation number and size for all analysis except foot-of-wave pulse velocity where pulse wave velocity values were similar. The study did not allow for minor differences in wall thickness to be evaluated. Increasing axial pre-tension has been reported to lower circumferential stiffness in elastomeric tubes⁶⁴ and this effect would be expected to lower pulse wave velocity.⁶⁵ Conversely, effective circumferential stiffening away from the phantom midsection due to end fixation would increase the regional pulse wave velocity. While this aspect of phantom behavior was not examined, as pretension was consistent between designs and effects likely modest, pretension is unlikely to interfere with comparison of compliance⁶⁶ and pulse wave velocity⁶⁵ between designs or to previously reported pulse wave velocities obtained in 3D printed phantoms. Temperature effects were not investigated; during pulsatile data collection fluid temperature varied up to 1.7°C within designs and 8.1°C between designs (Table 4). Wall stiffness and pulse wave velocity would be expected vary inversely with temperature. However, the lowest pulse wave velocities were observed for design H (Figure 9(b)), which was tested at the lower end of the temperature range,

suggesting that design features rather than temperature caused the pulsatile behavior differences observed between phantoms.

Unlike water, blood is a non-Newtonian fluid with a slightly higher density and its viscosity varies with flow, temperature, and geometry.⁶⁷ Consequently, more sophisticated phantom based hemodynamic studies will benefit from the use of blood mimicking fluids such as glycerol solutions. Elastomers based on polyurethane and silicon are generally compatible with a broad range of chemicals and are commonly utilized in low modulus additive manufacturing techniques. The polyester-polyurethane compound used to produce the phantoms in this study is particularly resistant to fats and oils including glycerol, which combined with its excellent printing and bonding characteristics, make it well suited for development of structurally functional hemodynamic phantoms.

This study simply demonstrates the short-term potential to create more elaborate corrugated wall phantoms that may be useful for studying wave mechanics in distensible tubes. The immediate application of the structure function approach to other arterial phantom applications such as flow visualization is not obvious. However, by separating material properties from phantom wall elasticity, this approach expands the range of materials that can be used to create distensible phantoms, potentially including those with light characteristics suitable for visualization studies.

The observations from this study are compelling enough to encourage further development of the functional structure approach to 3D printed arterial phantoms. Of particular importance is expanding the nonlinear behavior pressure range beyond the 23–45 mmHg achieved in this study to encompass the broad range of normal and pathophysiologic conditions in both the pulmonic and systemic circulation of humans and animal models. Resolving long axis anisotropy, replicating axial-circumferential strain relationships and practical production of complex geometry including, tapering, positive and negative reflection sites, branching, and curvature are also essential developments. Avenues to pursue these objectives include corrugation design optimization using advanced design tools that integrate complex architectures with mathematical surface definitions,^{68,69} and implementation of light-based elastomer 3D printing processes which will allow production of more intricate corrugate features with better design fidelity than is currently achievable with fused filament fabrication techniques.⁷⁰

Conclusions

To the extent of the authors' knowledge, this work demonstrates the first successful direct 3D-printed production of a range of robust arterial phantoms with pulse wave velocities on the order of 1.5–5 m s⁻¹, less than half of previously reported wave speeds¹⁷ and

within the range of pulmonary artery pulse wave velocities reported in humans and other species.^{28,31,34,35} This result was achieved via corrugated wall designs that separated phantom function from the mechanical properties of the polyurethane polymer construction material by creating nonlinear circumferential springs in the phantom walls. Importantly, the phantoms demonstrated design driven nonlinear elastic behavior with walls that stiffened with increased pressure, matching the physiologic response of arteries.^{19,20} Continued development of phantom production techniques, mock circulatory systems and instrumentation may produce novel knowledge regarding arterial pulse wave mechanics.


Declaration of conflicting interests

The author(s) declared no potential conflicts of interest with respect to the research, authorship, and/or publication of this article.

Funding

The author(s) disclosed receipt of the following financial support for the research, authorship, and/or publication of this article: This work was supported by Equine Guelph [grant number 052835].

ORCID iD

Bruce Guest  <https://orcid.org/0000-0001-5921-2890>

Supplemental material

Supplemental material for this article is available online.

References

1. Segers P, O'Rourke MF, Parker K, et al. Towards a consensus on the understanding and analysis of the pulse waveform: results from the 2016 workshop on arterial hemodynamics: past, present and future. *Artery Res* 2017; 18: 75–80.
2. Wang JJ, O'Brien AB, Shrive NG, et al. Time-domain representation of ventricular-arterial coupling as a windkessel and wave system. *Am J Physiol Heart Circ Physiol* 2003; 284(4): H1358–H1368.
3. Parker KH. An introduction to wave intensity analysis. *Med Biol Eng Comput* 2009; 47(2): 175–188.
4. Safar ME and Struijker-Boudier HA. Cross-talk between macro- and microcirculation. *Acta Physiol* 2010; 198: 417–430.
5. Climie RED, Picone DS, Blackwood S, et al. Pulsatile interaction between the macro-vasculature and micro-vasculature: proof-of-concept among patients with type 2 diabetes. *Eur J Appl Physiol* 2018; 118(11): 2455–2463.
6. Weber T, O'Rourke MF, Lassnig E, et al. Pulse waveform characteristics predict cardiovascular events and mortality in patients undergoing coronary angiography. *J Hypertens* 2010; 28(4): 797–805.
7. Hametner B, Wassertheurer S, Hughes AD, et al. Reservoir and excess pressures predict cardiovascular events in high-risk patients. *Int J Cardiol* 2014; 171(1): 31–36.
8. Laurent S, Cockcroft J, Van Bortel L, et al. Expert consensus document on arterial stiffness: methodological issues and clinical applications. *Eur Heart J* 2006; 27(21): 2588–2605.
9. Zannoli R, Corazza I and Branzi A. Mechanical simulator of the cardiovascular system. *Phys Med* 2009; 25(2): 94–100.
10. Khir AW, Swalen MJP, Feng J, et al. Simultaneous determination of wave speed and arrival time of reflected waves using the pressure–velocity loop. *Med Biol Eng Comput* 2007; 45(12): 1201–1210.
11. Lillie JS, Liberson AS, Mix D, et al. Pulse wave velocity prediction and compliance assessment in elastic arterial segments. *Cardiovasc Eng Technol* 2015; 6(1): 49–58.
12. Kolyva C, Biglino G, Pepper JR, et al. A mock circulatory system with physiological distribution of terminal resistance and compliance: application for testing the intra-aortic balloon pump. *Artif Organs* 2012; 36(3): E62–E70.
13. Kung EO and Taylor CA. Development of a physical windkessel module to re-create in-vivo vascular flow impedance for in-vitro experiments. *Cardiovasc Eng Technol* 2011; 2(1): 2–14.
14. Papageorgiou GL and Jones NB. Physical modelling of the arterial wall. Part 1: testing of tubes of various materials. *J Biomed Eng* 1987; 9(2): 153–156.
15. Yazdi SG, Geoghegan PH, Docherty PD, et al. A review of arterial phantom fabrication methods for flow measurement using PIV techniques. *Ann Biomed Eng* 2018; 46(11): 1697–1721.
16. Ionita CN, Mokin M, Varble N, et al. Challenges and limitations of patient-specific vascular phantom fabrication using 3D polyjet printing. *Proc SPIE Int Soc Opt Eng* 2014; 9038: 90380M.
17. Biglino G, Verschuere P, Zegels R, et al. Rapid prototyping compliant arterial phantoms for in-vitro studies and device testing. *J Cardiovasc Magn Reson* 2013; 15: 2–7.
18. Knoops PGM, Biglino G, Hughes AD, et al. A mock circulatory system incorporating a compliant 3d-printed anatomical model to investigate pulmonary hemodynamics. *Artif Organs* 2017; 41(7): 637–646.
19. Avolio A. Arterial stiffness. *Pulse* 2013; 1(1): 14–28.
20. Chirinos JA. Arterial stiffness: basic concepts and measurement techniques. *J Cardiovasc Transl Res* 2012; 5(3): 243–255.
21. Pereira T, Correia C and Cardoso J. Novel methods for pulse wave velocity measurement. *J Med Biol Eng* 2015; 35(5): 555–565.
22. Greene ES and Gerson JI. Arterial pulse wave velocity: a limited index of systemic vascular resistance during normotensive anesthesia in dogs. *J Clin Monit* 1985; 1(4): 219–226.
23. Nogueira RB, Pereira LA, Basso AF, et al. Arterial pulse wave propagation velocity in healthy dogs by pulse wave Doppler ultrasound. *Vet Res Commun* 2017; 41(1): 33–40.
24. Kamoi S, Pretty C, Balmer J, et al. Improved pressure contour analysis for estimating cardiac stroke volume using pulse wave velocity measurement. *Biomed Eng Online* 2017; 16(1): 51.
25. de Beaufort HWL, Coda M, Conti M, et al. Changes in aortic pulse wave velocity of four thoracic aortic stent

- grafts in an ex vivo porcine model. *PLoS One* 2017; 12(10): e0186080.
26. Graf S, Craiem D, Barra JG, et al. Estimation of local pulse wave velocity using arterial diameter waveforms: experimental validation in sheep. *J Phys Conf Ser* 2011; 332: 012010.
 27. Vera L, De Clercq D, Van Steenkiste G, et al. Differences in ultrasound-derived arterial wall stiffness parameters and noninvasive blood pressure between Friesian horses and Warmblood horses. *J Vet Intern Med* 2020; 34(2): 893–901.
 28. Kopeć G, Moertl D, Jankowski P, et al. Pulmonary artery pulse wave velocity in idiopathic pulmonary arterial hypertension. *Can J Cardiol* 2013; 29(6): 683–690.
 29. Sanz J, Prat-Gonzalez S, Macaluso F, et al. 155 quantification of pulse wave velocity in the pulmonary artery in patients with pulmonary hypertension. *J Cardiovasc Magn Reson* 2008; 10(S1): A56.
 30. Friesen RM, Schäfer M, Ivy DD, et al. Proximal pulmonary vascular stiffness as a prognostic factor in children with pulmonary arterial hypertension. *Eur Heart J Cardiovasc Imaging* 2019; 20(2): 209–217.
 31. Bouwmeester JC, Belenkie I, Shrive NG, et al. Wave reflections in the pulmonary arteries analysed with the reservoir-wave model. *J Physiol* 2014; 592(14): 3053–3062.
 32. Bargainer JD. Pulse wave velocity in the main pulmonary artery of the dog. *Circ Res* 1967; 20(6): 630–637.
 33. Dwyer N, Yong AC and Kilpatrick D. Variable open-end wave reflection in the pulmonary arteries of anesthetized sheep. *J Physiol Sci* 2012; 62(1): 21–28.
 34. Zuckerman BD, Orton EC, Stenmark KR, et al. Alteration of the pulsatile load in the high-altitude calf model of pulmonary hypertension. *J Appl Physiol* 1991; 70(2): 859–868.
 35. Silva GTA, Guest BB, Gomez DE, et al. Development of a technique for determination of pulmonary artery pulse wave velocity in horses. *J Appl Physiol* 2017; 122(5): 1088–1094.
 36. Poole DC and Erickson HH. *Equine Sports Medicine and Surgery*. 2nd ed. London: Saunders, 2014, pp.667–694.
 37. Hall JE and Guyton AC. *Guyton and Hall textbook of medical physiology*. 12th ed. Philadelphia, PA: Saunders, 2011. pp.158.
 38. Cornelissen VA, Verheyden B, Aubert AE, et al. Effects of aerobic training intensity on resting, exercise and post-exercise blood pressure, heart rate and heart-rate variability. *J Hum Hypertens* 2010; 24(3): 175–182.
 39. Daida H, Allison TG, Squires RW, et al. Peak exercise blood pressure stratified by age and gender in apparently healthy subjects. *Mayo Clin Proc* 1996; 71(5): 445–452.
 40. Reece WO and Dukes. *Physiology of domestic animals*. 12th ed. Ithaca, NY: John Wiley & Sons, 2015. pp.231–233; 362–363.
 41. Kovacs G, Berghold A, Scheidl S, et al. Pulmonary arterial pressure during rest and exercise in healthy subjects: a systematic review. *Eur Respir J* 2009; 34(4): 888–894.
 42. Aggarwal S, Gross CM, Porcelli RJ, et al. Pulmonary hemodynamics. In: Parent RA (ed.) *Comparative biology of the normal lung*. San Diego, CA: Academic Press, 2015, pp.205–243, 2nd ed.
 43. Kane GC, Sachdev A, Villarraga HR, et al. Impact of age on pulmonary artery systolic pressures at rest and with exercise. *Echo Res Pract* 2016; 3(2): 53–61.
 44. Elkins RC and Milnor WR. Pulmonary vascular response to exercise in the dog. *Circ Res* 1971; 29(6): 591–599.
 45. Manohar M. Pulmonary vascular pressures during near-maximal exertion in horses. *Faseb Journal* 1993; 7(4): A611–A611.
 46. Guest B, Arroyo L and Runciman J. Direct 3D printing of polyurethane nonlinear distensible tubes using a fused filament fabrication technique. *Prog Addit Manuf* 2022; 7: 3–14.
 47. Mohammadi A and Floryan JM. Spectral algorithm for the analysis of flows in grooved channels. *Int J Numer Methods Fluids* 2012; 69(3): 606–638.
 48. Gloss D and Herwig H. Wall roughness effects in laminar flows: an often ignored though significant issue. *Exp Fluids* 2010; 49(2): 461–470.
 49. Han HC. A biomechanical model of artery buckling. *J Biomech* 2007; 40(16): 3672–3678.
 50. Savitzky A and Golay MJE. Smoothing and differentiation of data by simplified least squares procedures. *Anal Chem* 1964; 36(8): 1627–1639.
 51. Schafer R. What is a savitzky-golay filter? [Lecture Notes]. *IEEE Signal Process Mag* 2011; 28(4): 111–117.
 52. Guest B, Arroyo L, Viel L, et al. Ex vivo equine heart and lung perfusion system. *Biomed Eng Appl Basis Commun* 2015; 27(5): 1550045.
 53. Nabeel PM, Kiran VR, Joseph J, et al. Local pulse wave velocity: theory, methods, advancements, and clinical applications. *IEEE Rev Biomed Eng* 2020; 13: 74–112.
 54. Runciman J, McGregor M, Silva G, et al. A new statistical phase offset technique for the calculation of in vivo pulse wave velocity. *Artery Res* 2016; 13: 17–27.
 55. Ding X, Wang Y, Hao Y, et al. A new measure of pulse rate variability and detection of atrial fibrillation based on improved time synchronous averaging. *Comput Math Methods Med* 2021; 2021: 5597559.
 56. Hunter KS, Albiets JA, Lee PF, et al. In vivo measurement of proximal pulmonary artery elastic modulus in the neonatal calf model of pulmonary hypertension: development and ex vivo validation. *J Appl Physiol* 2010; 108(4): 968–975.
 57. Chesler NC, Thompson-Figueroa J and Millburne K. Measurements of mouse pulmonary artery biomechanics. *J Biomech Eng* 2004; 126(2): 309–314.
 58. Kim EJ, Park CG, Park JS, et al. Relationship between blood pressure parameters and pulse wave velocity in normotensive and hypertensive subjects: invasive study. *J Hum Hypertens* 2007; 21(2): 141–148.
 59. McKean LW. *Fatigue and tribological properties of plastics and elastomers*. 3rd ed. London: William Andrew, 2016. Vol. 372, pp.1–26.
 60. Lammers S, Scott D, Hunter K, et al. Mechanics and function of the pulmonary vasculature: implications for pulmonary vascular disease and right ventricular function. *Compr Physiol* 2012; 2(1): 295–319.
 61. Nabavi M and Siddiqui K. A critical review on advanced velocity measurement techniques in pulsating flows. *Meas Sci Technol* 2010; 21(4): 042002.
 62. Nabeel PM, Sivaprakasam M and Joseph J. Variation in local pulse wave velocity over the cardiac cycle: in-vivo validation using dual-MPG arterial compliance probe. In: *13th Russian-German conference on biomedical engineering*, Aachen, Germany, 23–25 May 2018, RWTH-2018-224393.
 63. Borlotti A, Li Y, Parker KH, et al. Experimental evaluation of local wave speed in the presence of reflected waves. *J Biomech* 2014; 47(1): 87–95.

64. Horný L, Chlup H, Kužma J, et al. Inflation-extension behaviour of 3D printed elastomer tubes and their constitutive description. *Bioprinting* 2022; 25: e00192.
65. Horný L and Kužma J. Pressure pulse wave velocity and axial prestretch in arteries. In: *World congress on medical physics and biomedical engineering 2018* (eds L Lhotska, L Sukupova and I Lacković), Singapore, 2018, IFMBE Proceedings, vol. 68/2, pp.665–669. Singapore: Springer.
66. van der Bruggen MM, Reesink KD, Spronck PJM, et al. An integrated set-up for ex vivo characterisation of biaxial murine artery biomechanics under pulsatile conditions. *Sci Rep* 2021; 11(1): 2671.
67. Baskurt OK and Meiselman HJ. Blood rheology and hemodynamics. *Semin Thromb Hemost* 2003; 29(5): 435–450.
68. McNeel R. Grasshopper - alternative modeling with Rhino; 2010. www.grasshopper3d.com (accessed 3 September 2021).
69. Gleadall A. Fullcontrol gcode designer: open-source software for unconstrained design in additive manufacturing. *Addit Manuf* 2021; 46: 102109.
70. Zhao T, Yu R, Li S, et al. Superstretchable and processable silicone elastomers by digital light processing 3d printing. *ACS Appl Mater Interfaces* 2019; 11(15): 14391–14398.